Stability Assessment of DFIG Subsynchronous Oscillation Based on Energy Dissipation Intensity Analysis

Jing Ma, *Senior Member, IEEE*, and Yaqi Shen, *Member, IEEE*

***Abstract*—Concerning the subsynchronous oscillation caused by the integration of doubly-fed induction generator (DFIG) to the power grid via the series compensation circuit, a method to assess the stability of subsynchronous oscillation based on the dissipation intensity is proposed in this article. First, the transient energy that DFIG generates in one oscillation period is defined as the dynamic energy of DFIG, and the model of DFIG dynamic energy containing internal control and external networks is constructed. And then, according to the Lyapunov stability theory, the negative gradient of dynamic energy is defined as the dissipation intensity, which reflects the dissipation effect of DFIG on the energy generated during oscillation. On this basis, the effect of the series compensation degree, phase-locked loop, and converter control parameters on subsynchronous oscillation is assessed, and real-time assessment of the stability level of DFIG-integrated power system is realized. Finally, a simulation model is built in RT-LAB to verify the proposed method. Simulation results demonstrate that the stability level of the system can be assessed accurately according to the value of dissipation intensity. When the value of dissipation intensity is positive, system oscillation converges. When the dissipation intensity is zero, the system oscillates with constant-amplitude oscillation. When the value of dissipation intensity is negative, system oscillation diverges.**

***Index Terms*—Dissipation intensity, doubly-fed induction generator (DFIG), dynamic energy, phase-locked loop (PLL), subsynchronous oscillation.**

I. Introduction

IN RECENT years, as the penetration rate of wind generation keeps increasing when doubly-fed wind farm is transmitted via the series compensation system, subsynchronous oscillation has occurred ever more frequently as well as disconnection of wind farm from power grid, which greatly endangers the safe and stable operation of power system [1], [2]. Therefore, it is urgent to study methods to identify the developing trend of oscillation fast and effectively and assess system stability level online, thus providing reliable real-time stability criteria for wind farm control and power grid dispatching.

Currently, doubly-fed induction generator (DFIG) stability assessment methods mainly include offline assessment methods and online assessment methods. Offline assessment estimates the generator-grid resonance point and damping level through theoretical model calculation. Existing offline assessment methods can be categorized into the impedance-frequency scanning method, eigenvalue analysis method, and complex torque coefficient method. The impedance-frequency scanning analysis method identifies the resonance point by depicting the spectrum characteristics of DFIG and grid in a subsynchronous frequency band and then determines system stability according to the Nyquist criterion [3]–[7]. In [6], by constructing the positive-sequence and negative-sequence impedance models of the system based on the impedance analysis method, the stability of the system is analyzed qualitatively according to the Nyquist stability criterion. Huakun *et al*. [7] uses *dq*–axis impedance analysis and builds the RLC equivalent circuit near the resonance point so that the stability level of the system is identified quantitatively. The eigenvalue analysis method obtains the oscillation mode and damping information by calculating the eigenvalues of the full model of DFIG-grid system [8], [9]. In [9], the damping of oscillation mode in subsynchronous frequency is calculated quantitatively through eigenvalue analysis, thus realizing stability assessment of power system integrated with wind generation. The complex torque coefficient analysis method identifies whether subsynchronous oscillation will occur in the system according to the value of net damping coefficient [10], [11]. Tabesh *et al*. [11] derive the stability criteria of subsynchronous oscillation according to the relationship between the phases of stator/rotor torque and speed using the complex torque coefficient method. However, the above methods can only obtain offline stability criteria and are incapable of online stability assessment in the full-time domain. Besides, most of the above methods are based on the full-order model of power system integrated with wind generation, thus, are not applicable to the large-scale power system. Existing online stability assessment methods mainly include time-domain simulation analysis methods and online oscillation monitoring methods based on Fourier transformation,

Manuscript received 29 May 2019; revised 20 August 2019 and 27 October 2019; accepted 17 December 2019. Date of publication 24 December 2019; date of current version 22 April 2020. This work was supported in part by the National Key Research and Development Program of China under Grant 2018YFB0904003, in part by the National Natural Science Foundation of China under Grant 51777070, in part by Chinese Universities Scientific Fund under Grant 2018JQ01, and in part by Chinese Universities Scientific Fund under Grant 2018ZD01. Recommended for publication by Associate Editor M. Molinas. *(Corresponding author: Jing Ma.)*

The authors are with the State Key Laboratory of Alternate Electrical Power System with Renewable Energy Sources, North China Electric Power University, Beijing 102206, China (e-mail: hdmajing@163.com; jsntsyq1994@163.com).

This article has supplementary downloadable material available at http://ieeexplore.ieee.org, provided by the authors

Color versions of one or more of the figures in this article are available online at http://ieeexplore.ieee.org.

Digital Object Identifier 10.1109/TPEL.2019.2962217

wavelet transformation, etc. Time-domain analysis methods analyze the dynamic characteristic of the system according to the time-domain response curves of system state variables obtained by using numerical integration to solve the dynamic differential equation of system [9], [12]. However, time-domain methods can only provide the responses of variables and cannot assess the stability level of system oscillation. Besides, a large amount of computation is involved in solving a nonlinear differential equation, thus time-domain methods are not applicable to the stability analysis of large-scale power system. Fourier transformation is widely used to analyze the oscillation frequency, which can realize the decomposition of measured signals in the frequency domain, but is not applicable to signals with strong nonlinear characteristics generated in the power system [13]. Wavelet transformation is a time-frequency analysis method applicable to signals with strong nonlinear characteristics, which can track the variation process of system oscillation frequency with small computation amount and high computation speed. However, wavelet transformation can only decompose the signal in a certain frequency band, but cannot extract the characteristic of the signal at any specific frequency [14], [15]. The above three categories of online stability analysis methods can be applied to both big-disturbance and small-disturbance cases for real-time monitoring of system oscillation. However, these methods focus on signal analysis and the identification of attenuation coefficient and oscillation frequency concerning certain electrical variables, and cannot assess the overall stability level of the system after oscillation occurs.

Concerning the above problems, a method to assess the stability level of the power system with DFIG integration based on dissipation intensity is proposed in this article. First, the transient energy that DFIG generates in one oscillation period is defined as the dynamic energy of DFIG, and the model of dynamic energy at the terminal of DFIG is constructed. Furthermore, according to the Lyapunov stability theory, the negative gradient of dynamic energy is defined as the dissipation intensity, which characterizes the variation trend of system overall energy during oscillation and reflects the dissipation effect of DFIG on the energy generated during oscillation, i.e., the overall stability level of system. And then, by analyzing the effects of converter control parameters, phase-locked loop (PLL) control parameters, and grid-side line parameters on the dissipation intensity, the assessment of effect of system parameters on the stability level of DFIG subsynchronous oscillation is explored. On this basis, by measuring the real-time information of dynamic energy at the terminal of DFIG, the occurring and developing of system subsynchronous oscillation is monitored, and the dissipation intensity is calculated, thus real-time assessment of the stability level of DFIG-integrated power system is realized. Finally, simulation tests in RT-LAB based on network parameters of a real wind farm verify the correctness and effectiveness of the proposed method.

II. DFIG Dynamic Energy Model

A. Model of DFIG Terminal Dynamic Energy

Based on the node current equation, system energy function can be constructed [9]. Integration of node voltage, generator injection current, and load current along system trajectory yields

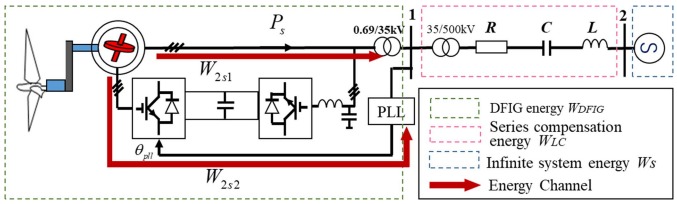

Fig. 1. Structure of DFIG-integrated power system.

the energy injected to bus i, as well as the conservation of system's overall energy

$$W = \int \mathrm{Im}((\boldsymbol{I}_i{}^*)^T d\boldsymbol{U}_i) \int \mathrm{Im}(((\boldsymbol{Y}\boldsymbol{U}_B - \boldsymbol{I}_G + \boldsymbol{I}_L)^*)^T d\boldsymbol{U}_B) = 0 \quad (1)$$

where $\boldsymbol{Y}$ is system admittance matrix, and $\boldsymbol{U}_B$ is the column vector of bus voltage. $\boldsymbol{I}_G$ and $\boldsymbol{I}_L$ are, respectively, the column vectors of injection current of generator nodes and load nodes. Im represents extracting the imaginary part of a complex.

The DFIG-integrated power system contains three parts, i.e., DFIG, the series compensation circuit, and the infinite bus system, as shown in Fig. 1. According to (1), the voltage of infinite bus system is constant, i.e., the energy at the terminal of bus 2 W_s is 0, thus energy interaction only exists between DFIG and the series compensation circuit, the energy conservation of which is expressed as

$$W_{\mathrm{DFIG}} + W_{LC} = 0 \quad (2)$$

where W_{DFIG} is the transient energy generated by DFIG, and W_{LC} is the transient energy generated by the series compensation circuit.

For spontaneous subsynchronous oscillation, DFIG as the oscillating source generates transient energy, which is then absorbed by the line. The more energy interacted between DFIG and the line, the more acutely the system oscillates. The interaction energy is determined by the transient energy of DFIG. Therefore, by analyzing the transient energy at the terminal of DFIG, the stability of subsynchronous oscillation can be identified.

In this article, the transient energy that DFIG generates in one oscillation period is defined as the dynamic energy of DFIG. According to (1), the dynamic energy that DFIG generates at any moment can be expressed as

$$W_{DFIG}(t) = \int_t^{t+\frac{2\pi}{\omega}} \mathrm{Im}\,(I_G^* dU_G) \quad (3)$$

where I_G and U_G are, respectively, the xy-axis components of voltage and current at the output terminal of DFIG. An oscillation period is selected as the interval of integration, and the integration value represents the instantaneous value of dynamic energy.

Transformation of (3) to dq–axis yields

$$\int_t^{t+\frac{2\pi}{\omega}} \mathrm{Im}(\boldsymbol{I}_{\boldsymbol{G}}^* d\boldsymbol{U}_G) = \int_t^{t+\frac{2\pi}{\omega}} (\boldsymbol{I}_d \cos\theta - \boldsymbol{I}_q \sin\theta)\, d\,(\boldsymbol{U}_d \sin\theta + \boldsymbol{U}_q \cos\theta)$$

$$
\begin{aligned}
&+\int_{t}^{t+\frac{2\pi}{\omega}}\left(\boldsymbol{I}_d\sin\theta+\boldsymbol{I}_q\cos\theta\right)d\left(\boldsymbol{U}_d\cos\theta-\boldsymbol{U}_q\sin\theta\right)\\
&=\int_{t}^{t+\frac{2\pi}{\omega}}I_d dU_q-I_q dU_d+P_e d\theta\\
&=\int_{t}^{t+\frac{2\pi}{\omega}}\left(\Delta i_d+i_{d0}\right)d\left(\Delta u_q+u_{q0}\right)\\
&\quad-\left(\Delta i_q+i_{q0}\right)d\left(\Delta u_d+u_{d0}\right)\\
&\quad+\int_{t}^{t+\frac{2\pi}{\omega}}\left(\Delta P_e+P_{e0}\right)d\left(\Delta\theta+\theta_0\right) \qquad (4)
\end{aligned}
$$

where P_e is DFIG output active power. θ is the angular difference between xy coordinate system, and dq coordinate system, which also represents the phase-locked angle of PLL. U_d, U_q, I_d, and I_q are, respectively, the *d*-axis and *q*-axis components of voltage and current at the output terminal of DFIG. ω is the oscillation frequency in *dq* coordinate system. Subscript "0" represents the steady-state value of the corresponding variable; "Δ" represents the variation of the corresponding variable from the steady-state value.

It can be seen from (4) that by measuring the information of terminal voltage, current, and power, DFIG terminal dynamic energy can be calculated. However, since the measured information of electrical variables contains a steady-state component that is irrelevant to oscillation, the dynamic energy obtained in (4) cannot accurately reflect the energy accumulation process during subsynchronous oscillation. To reduce the effect of steady-state component, replace each variable in (4) with the variation of the corresponding variable from the steady-state value, thus DFIG dynamic energy can be further expressed as

$$
\begin{aligned}
\Delta\boldsymbol{W}_{DFIG}&=\int_{t}^{t+\frac{2\pi}{\omega}}\Delta i_d d\Delta u_q-\Delta i_q d\Delta u_d\\
&\quad+\int_{t}^{t+\frac{2\pi}{\omega}}\Delta P_e d\Delta\theta=\Delta\boldsymbol{W}_1+\Delta\boldsymbol{W}_2. \qquad (5)
\end{aligned}
$$

According to (5), DFIG dynamic energy is composed of two parts

$$
\begin{aligned}
\Delta W_1&=\int_{t}^{t+\frac{2\pi}{\omega}}\Delta i_d d\Delta u_q-\Delta i_q d\Delta u_d\\
\Delta W_2&=\int_{t}^{t+\frac{2\pi}{\omega}}\Delta P_e d\Delta\theta \qquad (6)
\end{aligned}
$$

where ΔW_1 is the dynamic energy directly determined by voltage and current at the output terminal of DFIG. ΔW_2 is the dynamic energy directly determined by PLL and active power.

Next, we will analyze these two energy components separately.

B. Dynamic Energy ΔW_1 Directly Determined by Voltage and Current at the Output Terminal of DFIG

According to (6), during oscillation, the dynamic energy generated by transmission line is mainly affected by the *d*-axis and *q*-axis components of DFIG terminal voltage and current. Thus, the detailed expressions of *d*-axis and *q*-axis components of DFIG stator voltage and current are analyzed first.

When subsynchronous and super-synchronous current disturbance signals with frequency of ω_{1-} and ω_{1+} appear in the system, the variation of DFIG terminal phase current can be expressed as

$$
\Delta i_s=I_-\cos\left(\omega_{1-}t+\varphi_{i-}\right)+I_+\cos\left(\omega_{1+}t+\varphi_{i+}\right). \qquad (7)
$$

According to (7), the variation of voltage after the subsynchronous and super-synchronous currents flow through the series compensation circuit, i.e., the variation of voltage at DFIG grid-connecting point can be expressed as

$$
\Delta u_s=U_-\cos\left(\omega_{1-}t+\varphi_{u-}\right)+U_+\cos\left(\omega_{1+}t+\varphi_{u+}\right) \qquad (8)
$$

where ω_{1-} and ω_{1+} are, respectively, the angular frequency of subsynchronous and super-synchronous voltage and current. U_-, U_+, I_-, and I_+ are, respectively, the amplitudes of subsynchronous and super-synchronous voltages and currents. φ_{u-} and φ_{u+} are the initial phase angles of subsynchronous and super-synchronous voltages. φ_{i-} and φ_{i+} are the initial phase angles of subsynchronous and super-synchronous currents. $U_+=I_+X_+$,$U_-=I_-X_-$,$\varphi_{u-}=\varphi_{i-}+\varphi_{RLC}$,and $\varphi_{u+}=\varphi_{i+}+\varphi_{RLC}$, where X_+, X_-, and φ_{RLC} are the impedance and phase angle of series compensation circuit in subsynchronous frequency and super-synchronous frequency, respectively.

Apply *dq* transformation to (7) and (8), so that

$$
\begin{cases}
\Delta u_d=U_-\cos\left(\omega t-\varphi_{u-}\right)+U_+\cos\left(\omega t+\varphi_{u+}\right)\\
\Delta i_d=I_-\sin\left(\omega t-\varphi_{i-}\right)+I_+\sin\left(\omega t+\varphi_{i+}\right)\\
\Delta u_q=-U_-\sin\left(\omega t-\varphi_{u-}\right)+U_+\sin\left(\omega t+\varphi_{u+}\right)\\
\Delta i_q=-I_-\sin\left(\omega t-\varphi_{i-}\right)+I_+\sin\left(\omega t+\varphi_{i+}\right)
\end{cases} \qquad (9)
$$

where $\omega=\omega_s-\omega_{1-}=\omega_{1+}-\omega_s$.

Apply (9) to ΔW_1 in (6), so that the dynamic energy of the transmission line can be obtained

$$
\begin{aligned}
\Delta W_1&=\int_{t}^{t+\frac{2\pi}{\omega}}\left[-I_-^2\omega R+I_+I_-R\omega\cos\left(\varphi_{i+}+\varphi_{i-}\right)\right]dt\\
&\quad+\int_{t}^{t+\frac{2\pi}{\omega}}I_+I_-X_{LC}\omega\sin\left(\varphi_{i+}+\varphi_{i-}\right)dt \qquad (10)
\end{aligned}
$$

where *R* is the resistance of the series compensation circuit, and X_{LC} is the capacitance and reactance of the series compensation circuit.

It can be seen from (10), ΔW_1 is the dynamic energy component transmitted to the machine through the transmission line and is only relative to transmission line parameters of the power grid. Therefore, it is also the dynamic energy component affected by line parameters.

C. Dynamic Energy ΔW_2 Directly Determined by PLL and the Active Power

According to (6), the dynamic energy of PLL is affected by the variation of DFIG output active power ΔP_e and the variation of phase-locked angle $\Delta\theta$.

The variation of phase-locked angle is mainly affected by PLL control parameters. According to three-phase synchronous phase-locked control structure [16], the expression of PLL output phase angle can be obtained

$$
\triangle\ \theta_{\mathrm{pll}}\approx-\int k_{p\theta}u_q dt-\iint k_{i\theta}u_q dtdt. \qquad (11)
$$

Since the integration operation does not change the oscillation frequency, according to (10) and (11), the variation of phase-locked angle is

$$\triangle\,\theta_{\rm pll} \approx A\_\sin(\omega t+\varphi_{\theta-}) - A_+\sin(\omega t+\varphi_{\theta+}) \tag{12}$$

where A_-, A_+, $\varphi_{\theta-}$, and $\varphi_{\theta+}$ represent the amplitude and phase angle of $\triangle\,\theta_{\rm pll}$ in subsynchronous frequency and super-synchronous frequency, the detailed expressions of which are shown as

$$\begin{aligned} A_{+/-} &= U_{+/-}\times\left|\frac{k_{p\theta}s+k_{i\theta}}{s^2-U_{sq0}(k_{p\theta}s+k_{i\theta})}\right|_{s=j\omega} \\ &= U_{+/-}K_{pll} \\ \varphi_{\theta+/-} &= -\varphi_{U+/-}+\arctan\frac{\omega k_{p\theta}}{k_{i\theta}}. \end{aligned} \tag{13}$$

DFIG output active power ΔP_e is composed of grid-side active power and stator active power. Therefore, ΔW_2 has two energy channels, i.e., stator energy channel ΔW_{2s1}, as shown in Channel 1 in Fig. 1, and excitation energy channel ΔW_{2s2}, as shown in Channel 2 in Fig. 1. The expression of ΔW_2 is

$$\begin{aligned} W_2 &= W_{2s1}+W_{2s2} \\ &= \int_t^{t+\frac{2\pi}{\omega}}\Delta P_s d\Delta\theta + \int_t^{t+\frac{2\pi}{\omega}}\Delta P_g d\Delta\theta. \end{aligned} \tag{14}$$

The detailed expressions of energy components in two channels are analyzed below.

1) Stator Energy Channel: The variation of active power can be expressed with voltage and current as

$$\begin{aligned} \Delta P_s &= I_{sd0}\Delta u_{sd}+I_{sq0}\Delta u_{sq}+U_{sd0}\Delta i_{sd} \\ &\quad +\Delta i_{sd}\Delta u_{sd}+\Delta i_{sq}\Delta u_{sq} \end{aligned} \tag{15}$$

where I_{sd0}, I_{sq0}, and U_{sd0} are the initial values of d-axis and q-axis components of DFIG stator voltage and current.Δu_{sd}, Δu_{sq}, Δi_{sd}, and Δi_{sq} are the variation of d-axis and q-axis components of DFIG stator voltage and current.

Applying (10) and (15) to (14), the expression of energy in the stator channel can be obtained

$$\begin{aligned} \Delta W_{2s1} &= \int_t^{t+\frac{2\pi}{\omega}}\left(I_{sd0}\omega\frac{\cos\varphi_c}{2}+I_{sq0}\omega\frac{\sin\varphi_c}{2}\right)A\_U\_dt \\ &\quad +U_{sd0}\omega\frac{\cos(\varphi_c-\varphi_{RLC})}{2}A\_I\_dt \\ &\quad -\int_t^{t+\frac{2\pi}{\omega}}\left[\left(I_{sd0}\omega\frac{\cos\varphi_c}{2}+I_{sq0}\omega\frac{\sin\varphi_c}{2}\right)A_+U_+\right. \\ &\quad \left.+U_{sd0}\omega\frac{\cos(\varphi_c-\varphi_{RLC})}{2}A_+I_+\right]dt \\ &\quad +\int_t^{t+\frac{2\pi}{\omega}}\omega K_{pll}U\_U_+\sin\varphi_c\left[I_{sd0}\sin(\varphi_{u+}+\varphi_{u-})\right. \\ &\quad \left.-I_{sq0}\cos(\varphi_{u+}+\varphi_{u-})\right]dt. \end{aligned} \tag{16}$$

2) Excitation Energy Channel: In (14), grid-side converter output active power ΔP_g in excitation channel energy $\int_t^{t+\frac{2\pi}{\omega}}\Delta P_g d\Delta\theta$ can be expressed as

$$\Delta P_g = \Delta P_r - \Delta P_{\rm dc}. \tag{17}$$

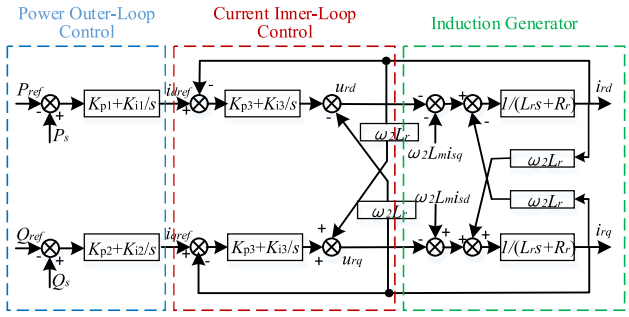

Fig. 2. Rotor-side control structure.

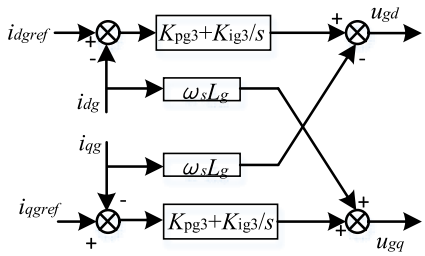

Fig. 3. Grid-side control structure.

Since the time scale of subsynchronous oscillation is much smaller than that of DC bus voltage, the dynamic variation of dc bus capacitance during oscillation is not considered in this article, i.e.,$\Delta P_{\rm dc}=0$. Thus, according to (17), the excitation channel energy can be written as

$$W_{2s2} = \int_t^{t+\frac{2\pi}{\omega}}\Delta P_g d\Delta\theta = \int_t^{t+\frac{2\pi}{\omega}}\Delta P_r d\Delta\theta. \tag{18}$$

It can be seen from (18) that the excitation channel energy is jointly affected by rotor-side converter control and grid-side converter control. Therefore, rotor-side converter excitation channel energy $\int_t^{t+\frac{2\pi}{\omega}}\Delta P_r d\Delta\theta$ and grid-side converter excitation channel energy $\int_t^{t+\frac{2\pi}{\omega}}\Delta P_g d\Delta\theta$ are studied, respectively.

For rotor-side converter excitation channel energy, when the flow direction of W_{2s2} in Fig. 1 is taken as the positive direction, DFIG rotor active power ΔP_r can be expressed as

$$\Delta P_r = -(I_{rd0}\Delta u_{rd}+U_{rd0}\Delta i_{rd}+\Delta i_{rd}\Delta u_{rd}+\Delta i_{rq}\Delta u_{rq}) \tag{19}$$

where I_{rd0} and U_{rd0} are, respectively, the initial values of d-axis components of rotor-side voltage and current, which are constant.Δu_{rd}, Δu_{rq}, Δi_{rd}, and Δi_{rq} are the variation of d-axis and q-axis components of rotor-side voltage and current.

The control structure of the rotor-side converter of wind turbine containing induction generator is shown in Fig. 2 [16]. According to the inner-loop and outer-loop control blocks, the variation of rotor voltage, after rotor current flows through the rotor-side converter Δu_{rd} and Δu_{rq}, can be expressed as

$$\begin{cases} \Delta u_{rd} = \left(K_{p3}+\frac{K_{i3}}{s}\right)\left[\left(K_{p1}+\frac{K_{i1}}{s}\right)\Delta P_s-\Delta i_{rd}\right] \\ \qquad\qquad -\omega_2 L_r\Delta i_{rq} \\ \Delta u_{rq} = \left(K_{p3}+\frac{K_{i3}}{s}\right)\left[\left(K_{p2}+\frac{K_{i2}}{s}\right)\Delta Q_s-\Delta i_{rq}\right] \\ \qquad\qquad +\omega_2 L_r\Delta i_{rd} \end{cases} \tag{20}$$

where L_r is the inductance of generator rotor, L_m is the excitation inductance, ω_r is rotor speed, $\omega_2 = \omega_s - \omega_r$.$K_{p1}$, K_{i1}, and K_{p2}, and K_{i2} are, respectively, the proportion and integration gain coefficients of power outer loop. K_{p3} and K_{i3} are the proportion and integration gain coefficients of current inner loop.

When the variation of stator flux and the stator resistance are neglected, the expression of stator power can be obtained according to the relationship between stator-side voltage, flux, and current [18]

$$\begin{cases} \Delta P_s = -\frac{L_m}{L_s} U_s \Delta i_{rd} \\ \Delta Q_s = -\frac{U_s^2}{\omega_s L_s} - \frac{L_m}{L_s} U_s \Delta i_{rq} \end{cases}. \tag{21}$$

Applying (21) to (20) yields (22), shown at the bottom of this page.

It can be seen from the control block of the induction generator in Fig. 2 that the variation of rotor current will, in turn, act on rotor windings and cause rotor current to vary. Rotor voltage and current considering the dynamic characteristic of the induction generator can be expressed as

$$\begin{cases} \Delta u_{rd} = R_r \Delta i_{rd} - \frac{L_r L_s - L_m^2}{L_s} \omega_2 \Delta i_{rq} + a_2 s \Delta i_{rd} \\ \Delta u_{rq} = R_r \Delta i_{rq} + \frac{L_r L_s - L_m^2}{L_s} \omega_2 \Delta i_{rd} + a_2 s \Delta i_{rq}. \end{cases} \tag{23}$$

Combining (22) and (23) and solving the first-order linear differential equations, the variation of rotor current can be obtained

$$\begin{cases} \Delta i_{rd} = aI_- \sin(\omega t - \varphi_{i-} + \varphi) + aI_+ \sin(\omega t - \varphi_{i+} + \varphi) \\ \Delta i_{rq} = aI_- \cos(\omega t - \varphi_{i-} + \varphi) + aI_+ \cos(\omega t - \varphi_{i+} + \varphi) \end{cases} \tag{24}$$

where $a = \frac{(R_r - U_s K_{p1} K_{p3})\omega_1^2 + U_s K_{i1} K_{i3}}{\omega^2 R_r \cos\varphi - (\frac{L_m^2 - L_r L_s}{L_s})^2 \omega^2 (\omega_s - \omega_r)}$

$$\varphi = \arctan \frac{\omega U_s (K_{p1} K_{i3} + K_{i1} K_{p3})}{\omega^2 (R_r - U_s K_{p1} K_{p3}) + U_s K_{i1} K_{i3}}.$$

Applying (19)–(24) to (18), the expression of rotor-side excitation channel energy can be obtained as (25), shown at the bottom of this page.

In grid-side converter excitation channel energy, the expression of DFIG grid-side converter active power ΔP_g can be derived in the way similar to that of rotor-side active power and can be written as

$$\Delta P_g = -(I_{gd0} \Delta u_{gd} + U_{gd0} \Delta i_{gd} + \Delta i_{gd} \Delta u_{gd} + \Delta i_{gq} \Delta u_{gq}) \tag{26}$$

where I_{gd0}, I_{gq0}, U_{gd0}, and U_{gq0} are, respectively, the initial values of d-axis and q-axis components of grid-side voltage and current, which are constant.Δu_{gd}, Δu_{gq}, Δi_{gd}, and Δi_{gq}, respectively, are the variation of d-axis and q-axis components of grid-side voltage and current.

The variation of dc bus voltage and the effect of grid-side converter outer-loop control are not considered in this article, thus according to the structure of grid-side converter inner-loop control [17], the expression of grid-side voltage can be written as

$$\begin{aligned} \Delta u_{gd} &= -\left(K_{pg3} + \frac{K_{ig3}}{s}\right) \Delta i_{gd} - \omega_s L_g \Delta i_{gq} \\ \Delta u_{gq} &= -\left(K_{pg3} + \frac{K_{ig3}}{s}\right) \Delta i_{gq} + \omega_s L_g \Delta i_{gd}. \end{aligned} \tag{27}$$

Applying (26) and (27) to (18), the expression of grid-side converter excitation channel energy can be obtained

$$\begin{aligned} \Delta W_{2s2} = &\int_{t_0}^{t_0 + \frac{2\pi}{\omega}} \frac{K_{pg3} I_{dg0} \omega + U_{dg0}}{2} \\ &\times (I_- U_- - I_+ U_+) K_{\text{pll}} \cos(\varphi_{i-} + \varphi_{\theta-}) \, dt \\ &- \int_{t_0}^{t_0 + \frac{2\pi}{\omega}} I_{dg0} \frac{K_{ig3} - \omega \omega_s L_g}{2} \\ &\times (I_- U_- - I_+ U_+) K_{\text{pll}} \sin(\varphi_{i-} + \varphi_{\theta-}) \, dt \end{aligned} \tag{28}$$

where L_g is the output reactance of the grid-side converter, K_{pg3} and K_{ig3} are the proportion and integration coefficients of grid-side converter power outer loop, respectively, and I_{dg0} is the initial value of d-axis components of grid-side current.

$$\begin{cases} \Delta u_{rd} = \left(K_{p3} + \frac{K_{i3}}{s}\right) \left[-\left(K_{p1} + \frac{K_{i1}}{s}\right) \frac{L_m}{L_s} U_s \Delta i_{rd} - \Delta i_{rd} \right] - \omega_2 L_r \Delta i_{rq} \\ \Delta u_{rq} = \left(K_{p3} + \frac{K_{i3}}{s}\right) \left[-\left(K_{p2} + \frac{K_{i2}}{s}\right) \left(\frac{L_m}{L_s} U_s \Delta i_{rq} + \frac{U_s^2}{\omega_s L_s} \right) - \Delta i_{rq} \right] + \omega_2 L_r \Delta i_{rd} \end{cases} \tag{22}$$

$$\begin{aligned} \Delta W_{2s2} = &\frac{1}{2} \int_{t_0}^{t_0 + \frac{2\pi}{\omega}} I_{dr0} (I_- U_- - I_+ U_+) K_{\text{pll}} \cos(\varphi_{i-} + \varphi_{\theta-}) K_{p3} \omega \left(\frac{L_m}{L_s} U_s K_{p1} + 1 \right) dt \\ &- \frac{1}{2} \int_{t_0}^{t_0 + \frac{2\pi}{\omega}} I_{dr0} (I_- U_- - I_+ U_+) K_{\text{pll}} \sin(\varphi_{i-} + \varphi_{\theta-}) \frac{L_m}{L_s} U_s \omega K_{p1} K_{i3} dt \\ &- \frac{1}{2} \int_{t_0}^{t_0 + \frac{2\pi}{\omega}} I_{dr0} (I_- U_- - I_+ U_+) K_{\text{pll}} \cos(\varphi_{i-} + \varphi_{\theta-}) \left(\frac{L_m}{L_s} U_s \frac{K_{i3} K_{i1}}{\omega} \right) dt \\ &- \frac{1}{2} \int_{t_0}^{t_0 + \frac{2\pi}{\omega}} I_{dr0} (I_- U_- - I_+ U_+) K_{\text{pll}} \sin(\varphi_{i-} + \varphi_{\theta-}) \left(\frac{L_m}{L_s} U_s K_{i1} K_{p3} + K_{i3} - \omega \omega_2 L_r \right) dt \\ &- \frac{1}{2} \int_{t_0}^{t_0 + \frac{2\pi}{\omega}} U_{dr0} (I_- U_- - I_+ U_+) K_{\text{pll}} \sin(\varphi_{i-} + \varphi_{\theta-}) \frac{(R_r - U_s K_{p1} K_{p3}) \omega_1^2 + U_s K_{i1} K_{i3}}{\omega^2 R_r \cos\varphi - \left(\frac{L_m^2 - L_r L_s}{L_s} \right)^2 \omega^2 (\omega_s - \omega_r)} dt \end{aligned} \tag{25}$$

III. Assessment of Stability Level of Subsynchronous Oscillation in DFIG-Integrated System

The accumulation process of dynamic energy can reflect the stability of the power system. In order to analyze the stability level of subsynchronous oscillation quantitatively, the Lyapunov stability criteria are used to establish a criterion for the stability assessment of subsynchronous oscillation, a stability level online assessment scheme is proposed, and the degree in which different parameters affect system stability level is analyzed.

A. Subsynchronous Oscillation Stability Assessment Criteria

For the DFIG-integrated power system shown in Fig. 1, the overall energy is the dynamic energy caused by oscillation which is only interacted between DFIG and the line and can be represented by the dynamic energy that DFIG generates $\Delta W_{\mathrm{DFIG}}(t)$, which is constantly positive.

According to Lyapunov stability theory, for a free dynamic system, if the variation rate of system overall energy V ($V > 0$) with time $\dot{V}(x)$ is constantly negative, system overall energy will keep decreasing until it reaches the minimum value, i.e., the equilibrium state, and the system is stable. When $\Delta W_{\mathrm{DFIG}}(t)$ gradually decreases, i.e., when $\Delta \dot{W}_{\mathrm{DFIG}}(t)$ is constantly negative, system's overall energy will keep decreasing until it reaches the minimum value, and the system will reach a stable state. If $\Delta W_{\mathrm{DFIG}}(t)$ gradually increases, $\Delta \dot{W}_{\mathrm{DFIG}}(t)$ is constantly positive, system's overall energy will keep increasing and the system will finally oscillate to an unstable state. According to the variable gradient method of Schultz–Gibson, the negative time gradient of $\Delta W_{\mathrm{DFIG}}(t)$ is defined as the dissipation intensity, which can quantitatively characterize the degree of increasing or decreasing of $\Delta W_{\mathrm{DFIG}}(t)$ and reflect the dissipation speed of system overall energy. The dissipation intensity is denoted as η, the definition of which is

$$\eta = -\nabla\left[\frac{|\Delta W_{\mathrm{DFIG}}(t) - \Delta W_{\mathrm{DFIG\_}av}|}{\left(\frac{1}{n}\sum_{t=1}^{n}\left(\Delta W_{\mathrm{DFIG}}(t) - \Delta W_{\mathrm{DFIG\_}av}\right)^2\right)^{\frac{1}{2}}}\right] \tag{29}$$

where $\nabla[\bullet]$ is the symbol of the gradient. The item inside $[\bullet]$ represents the normalization of dynamic energy on time scale in order to eliminate the difference in dynamic energy caused by disturbance.

According to (29), when $\eta > 0$, the dynamic energy that DFIG generates gradually decreases, and the system is stable. The bigger η is, the faster the dynamic energy decreases, the higher the system stability level is, and the faster system oscillation converges. When $\eta = 0$, the dynamic energy that DFIG generates is constant, and the system is critical stable with constant-amplitude oscillation. When $\eta < 0$, the dynamic energy that DFIG generates gradually increases, and the system stability level is negative. The smaller the η is, the faster the dynamic energy increases, and the more acutely subsynchronous oscillation diverges. Therefore, the stability level of DFIG subsynchronous oscillation can be assessed quantitatively according the value of η.

B. Online Stability Assessment Procedure

The dissipation intensity can be calculated according to the information of electrical variables at the terminal of DFIG directly, without referring to system network structure. Thus the online assessment of system stability level can be realized, the detailed procedure of which is as follows and the logical diagram of the proposed assessment scheme is shown in Fig. 4.

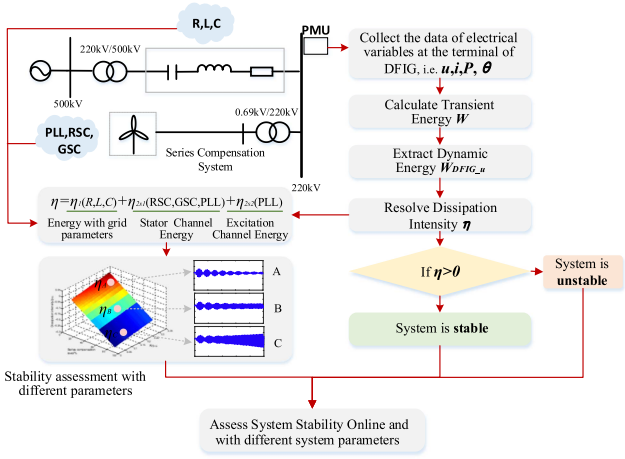

Fig. 4. Logical diagram of the proposed assessment scheme.

Step 1: Collect the data of electrical variables at the terminal of DFIG, i.e., the current, voltage, power, and phase-locked angle $\Delta i_d(k)$, $\Delta i_q(k)$, $\Delta u_d(k)$, $\Delta u_q(k)$, $\Delta P(k)$, $\Delta\theta(k)$, and calculate the variation of the measured values of these variables from the steady-state values. And then, the measured electrical variables in *abc*-axis are transformed to *dq*-axis through *abc-dq* transformation

$$\boldsymbol{x_{dq}} = \begin{bmatrix} \cos\theta_0 \cos(\theta_0 - 120°) & \cos(\theta_0 + 120°) \\ \sin\theta_0 \sin(\theta_0 - 120°) & \sin(\theta_0 + 120°) \end{bmatrix} \boldsymbol{x_{abc}}. \tag{30}$$

Discretizing (1) and combining the collected information of electrical variables, the variation of transient energy at the terminal of DFIG can be calculated

$$\begin{aligned} \Delta W(k) = {} & \frac{1}{2}\left[\Delta i_d(k) + \Delta i_d(k+1)\right]\left[\Delta u_q(k+1) - \Delta u_q(k)\right] \\ & - \frac{1}{2}\left[\Delta i_q(k) + \Delta i_q(k+1)\right]\left[\Delta u_d(k+1) - \Delta u_d(k)\right] \\ & + \frac{1}{2}\left[\Delta P(k) + \Delta P(k+1)\right]\left[\Delta\theta(k+1) - \Delta\theta(k)\right]. \end{aligned} \tag{31}$$

Applying (7), (8), and (12) to (1), the relationship between the variation of DFIG transient energy and the oscillation frequency can be obtained

$$\begin{aligned} \Delta W = {} & \int I_-\omega U_+ \cos(\varphi_{u+} + \varphi_{i-}) \\ & + I_-\omega U_- \cos(\varphi_{u-} - \varphi_{i-})\, dt \\ & - \int I_-\omega U_- \cos(2\omega t - \varphi_{i-} - \varphi_{u-}) \\ & - I_+\omega U_+ \cos(2\omega t + \varphi_{i+} + \varphi_{u+})\, dt \\ & - \int AI_{d0}\omega U_- \sin(\varphi_\theta + \varphi_{u-}) \\ & + AI_{d0}\omega U_+ \sin(\varphi_\theta - \varphi_{u+})\, dt \end{aligned}$$

$$
\begin{aligned}
&- \int AU_{d0}\omega I_{-}\sin\left(\varphi_{\theta}+\varphi_{i-}\right)\\
&+ AU_{d0}\omega I_{+}\sin\left(\varphi_{\theta}-\varphi_{i+}\right)dt\\
&- \int AI_{d0}\omega U_{-}\sin\left(2\omega t+\varphi_{\theta}-\varphi_{u-}\right)\\
&+ AI_{d0}\omega U_{+}\sin\left(2\omega t+\varphi_{\theta}+\varphi_{u+}\right)dt\\
&- \int AU_{d0}\omega I_{-}\sin\left(2\omega t+\varphi_{\theta}-\varphi_{i-}\right)\\
&+ AU_{d0}\omega I_{+}\sin\left(2\omega t+\varphi_{\theta}+\varphi_{i+}\right)dt. \qquad (32)
\end{aligned}
$$

It can be seen from (32) that $U_{-}(t)$ contains oscillation components with a frequency of 2ω, where $\omega=\omega_0-\omega_{-}$ is the oscillation frequency of *dq*-axis components of voltage and current. When ΔW exhibits ascending or descending trend in oscillation, the oscillation frequencies in the dynamic energy are detected using the Prony algorithm, and 1/2 of the dominant oscillation frequency is extracted as the frequency of system subsynchronous oscillation in *dq*-axis. Since the frequency of sub/super-synchronous oscillation studied in this article is in the frequency band of 2–100 Hz, the sampling frequency is selected to be above 200 Hz.

Step 2: Calculate the transient energy that DFIG generates in any oscillation period so that the expression of DFIG dynamic energy $\Delta W_{\mathrm{DFIG}}(k)$ can be obtained

$$
\begin{aligned}
\Delta W_{\mathrm{DFIG}}(k) =& \frac{1}{2}\left[\Delta i_d(k)+\Delta i_d(k+1)\right]\\
&\times\left[\Delta u_q(k+1)-\Delta u_q(k)\right]\\
&-\frac{1}{2}\left[\Delta i_q(k)+\Delta i_q(k+1)\right]\\
&\times\left[\Delta u_d(k+1)-\Delta u_d(k)\right]\\
&+\frac{1}{2}\left[\Delta P(k)+\Delta P(k+1)\right]\\
&\times\left[\Delta\theta(k+1)-\Delta\theta(k)\right] \qquad (33)
\end{aligned}
$$

where $T=N\frac{2\pi}{\omega}$, and *N* is the sampling frequency.

To eliminate the error in the amplitude of dynamic energy caused by different disturbances, the discretized dynamic energy is normalized as follows:

$$
\Delta W_{\mathrm{DFIG\_}u}(k)=\frac{\left|\Delta W_{\mathrm{DFIG}}(k)-\Delta W_{\mathrm{DFIG\_}av}\right|}{\left(\frac{1}{n}\sum_{t=1}^{n}\left(\Delta W_{\mathrm{DFIG}}(k)-\Delta W_{\mathrm{DFIG\_}av}\right)^2\right)^{\frac{1}{2}}} \qquad (34)
$$

where $\Delta W_{\mathrm{DFIG\_}av}$ is the mean value of dynamic energy.

Step 3: Apply the normalized dynamic energy $\Delta W_{\mathrm{DFIG\_}u}(k)$ to (38), so that dissipation intensity η can be calculated, the stability level of the system can be assessed according to the value of η. When $\eta>0$, the system is stable, and the bigger η is, the higher the stability level is. When $\eta=0$, the system is critical stable. When $\eta<0$, the stability level is negative and the system subsynchronous oscillation diverges

$$
\begin{aligned}
\eta=&-\frac{1}{N}\sum_{t=1}^{n}\\
&\times\frac{\Delta W_{\mathrm{DFIG\_}u}(k+nT)-\Delta W_{\mathrm{DFIG\_}u}(k+(n-1)T)}{t(nT)-t[(n-1)T]}. \qquad (35)
\end{aligned}
$$

It should be noted that, although the stability criteria of dissipation intensity proposed in this article are based on an infinite-bus system, it is also applicable to noninfinite system with DFIG integration. In the case of noninfinite system, energy conservation exists between the wind farm, line, and power grid; as the oscillation source, the wind farm generates dynamic energy, which is absorbed by the line and power grid; and the dynamic energy at the terminal of wind farm can still reflect the variation of system overall energy.

C. Energy Intensity Assessment With Different System Parameters

1) Grid Parameters: The dynamic energy generated by the transmission line is mainly affected by the series compensation degree and line resistance. Apply (10) to (29), so that the dissipation intensity of transmission line concerning subsynchronous oscillation can be obtained

$$
\begin{aligned}
\eta_1 =& \left[I_{-}\frac{dI_{-}}{dt}\omega R-I_{+}\frac{dI_{-}}{dt}\omega R\cos\left(\varphi_{i+}+\varphi_{i-}\right)\right]\Bigg|_{t_0}^{t_0+\frac{2\pi}{\omega}}\\
&+\left[I_{-}\frac{dI_{-}}{dt}\omega R-I_{-}\frac{dI_{+}}{dt}\omega R\cos\left(\varphi_{i+}+\varphi_{i-}\right)\right]\Bigg|_{t_0}^{t_0+\frac{2\pi}{\omega}}\\
&-I_{+}\frac{dI_{-}}{dt}X_{LC}\omega\sin\left(\varphi_{i+}+\varphi_{i-}\right)\Big|_{t_0}^{t_0+\frac{2\pi}{\omega}}\\
&-I_{-}\frac{dI_{+}}{dt}X_{LC}\omega\sin\left(\varphi_{i+}+\varphi_{i-}\right)\Big|_{t_0}^{t_0+\frac{2\pi}{\omega}} \qquad (36)
\end{aligned}
$$

where η_1 is the dissipation intensity generated by the transmission line.

In (29), the first item is the dissipation intensity generated by line resistance *R*, and the second item is the dissipation intensity generated by an *LC* series compensation system. Considering that the subsynchronous component is dominant in the DFIG connected system, $I_{-}|_{t_0}^{t_0+\frac{2\pi}{\omega}}>I_{+}|_{t_0}^{t_0+\frac{2\pi}{\omega}}$ and $\frac{dI_{-}}{dt}|_{t_0}^{t_0+\frac{2\pi}{\omega}}>\frac{dI_{+}}{dt}|_{t_0}^{t_0+\frac{2\pi}{\omega}}$, thus the resistance of transmission line *R* has positive dissipation intensity concerning subsynchronous oscillation. By increasing the value of *R*, the system stability level will improve and subsynchronous oscillation will converge. On the other hand, the *LC* series compensation system has negative dissipation intensity, and as the series compensation degree increases, *LC* will generate more negative dissipation intensity, thus lowering system stability level and aggravating the divergence of subsynchronous oscillation.

2) Rotor-Side Converter Control Parameters: According to the analysis in Chapter II, rotor-side converter control parameters affect the stability level of the DFIG-integrated power system mainly by changing the dissipation intensity of DFIG through the excitation channel energy.

Applying (25) to (29), the expression of rotor-side converter excitation channel dissipation intensity can be obtained as (37) shown at the bottom of this page.

Affected by the value of ω, the value of (37) is mainly determined by the first two items, i.e., the excitation channel dissipation intensity is mainly affected by rotor-side converter inner-loop proportion gain K_{p3}, outer-loop proportion gain K_{p1}, and inner-loop integration gain K_{i3}. According to (31), decreasing K_{p3} or increasing K_{i3} and K_{p1} can increase the excitation channel dissipation intensity, thus improving the stability level of DFIG sub/super-synchronous oscillation and accelerating the convergence of sub/super-synchronous oscillation.

3) Grid-Side Converter Control Parameters: Applying (28) to (29), the expression of grid-side converter excitation channel dissipation intensity can be obtained as follows:

$$\begin{aligned}\Delta\eta_{2s2} = &-\frac{K_{pg3}I_{dg0}\omega + U_{dg0}}{2}\left(I_{-}U_{-} - I_{+}U_{+}\right)\\ &K_{\mathrm{pll}}\cos\left(\varphi_{i-}+\varphi_{\theta-}\right)\Big|_{t_0}^{t_0+\frac{2\pi}{\omega}}\\ &+ I_{dg0}\frac{K_{ig3}-\omega\omega_s L_g}{2}\left(I_{-}U_{-} - I_{+}U_{+}\right)\\ &K_{\mathrm{pll}}\sin\left(\varphi_{i-}+\varphi_{\theta-}\right)\Big|_{t_0}^{t_0+\frac{2\pi}{\omega}}. \end{aligned} \tag{38}$$

It can be seen from (38) that, by reducing grid-side converter current inner-loop d-axis proportion parameter K_{pg3} or increasing current inner-loop integration coefficient K_{ig3}, the dissipation intensity of DFIG can be increased, thus the stability level of subsynchronous oscillation in DFIG-integrated power system can be improved.

It should be noted that, since the capacity of the grid-side converter is much smaller than that of the rotor-side converter, the reference value of current in the grid-side converter is much smaller than the reference value of current in the rotor-side converter, i.e., $I_{qg0} \ll I_{qr0}$ and $I_{dg0} \ll I_{dr0}$. According to (38), grid-side converter control parameters affect the dissipation intensity in a much smaller degree than rotor-side converter control parameters. Therefore, the stability level of DFIG subsynchronous oscillation is mainly affected by rotor-side converter control parameters.

4) PLL Parameters: According to the energy analysis in Chapter II, PLL affects the stability level of subsynchronous oscillation through the stator energy channel and excitation energy channel.

Applying (15) to (29), the dissipation intensity that PLL generates through the stator energy channel can be obtained as follows:

$$\begin{aligned}\eta_{2s1} = &-K_{\mathrm{pll}}\left(I_{sd0}\omega\cos\varphi_c + I_{sq0}\omega\sin\varphi_c\right)U_{-}\frac{dU_{-}}{dt}\Big|_{t_0}^{t_0+\frac{2\pi}{\omega}}\\ &- K_{\mathrm{pll}}U_{sd0}\omega\frac{\cos\left(\varphi_c-\varphi_{RLC}\right)}{2}\\ &\times\left(U_{-}\frac{dI_{-}}{dt}+I_{-}\frac{dU_{-}}{dt}\right)\Big|_{t_0}^{t_0+\frac{2\pi}{\omega}}\\ &+ K_{\mathrm{pll}}\left(I_{sd0}\omega\cos\varphi_c + I_{sq0}\omega\sin\varphi_c\right)U_{+}\frac{dU_{+}}{dt}\Big|_{t_0}^{t_0+\frac{2\pi}{\omega}}\\ &+ K_{\mathrm{pll}}U_{sd0}\omega\frac{\cos\left(\varphi_c-\varphi_{RLC}\right)}{2}\\ &\times\left(U_{+}\frac{dI_{+}}{dt}+I_{+}\frac{dU_{+}}{dt}\right)\Big|_{t_0}^{t_0+\frac{2\pi}{\omega}}\\ &- K_{\mathrm{pll}}\omega U_{-}\frac{dU_{+}}{dt}\sin\varphi_c\left[I_{sd0}\sin\left(\varphi_{u+}+\varphi_{u-}\right)\right.\\ &\left.-I_{sq0}\cos\left(\varphi_{u+}+\varphi_{u-}\right)\right]\Big|_{t_0}^{t_0+\frac{2\pi}{\omega}}\\ &- K_{\mathrm{pll}}\omega U_{+}\frac{dU_{-}}{dt}\sin\varphi_c\left[I_{sd0}\sin\left(\varphi_{u+}+\varphi_{u-}\right)\right.\\ &\left.-I_{sq0}\cos\left(\varphi_{u+}+\varphi_{u-}\right)\right]\Big|_{t_0}^{t_0+\frac{2\pi}{\omega}}. \end{aligned} \tag{39}$$

$$\begin{aligned}\Delta\eta_{2s2} = &-\frac{1}{2}I_{dr0}\left(I_{-}U_{-} - I_{+}U_{+}\right)K_{\mathrm{pll}}\cos\left(\varphi_{i-}+\varphi_{\theta-}\right)K_{p3}\omega\left(\frac{L_m}{L_s}U_s K_{p1}+1\right)\Big|_{t_0}^{t_0+\frac{2\pi}{\omega}}\\ &+\frac{1}{2}I_{dr0}\left(I_{-}U_{-} - I_{+}U_{+}\right)K_{\mathrm{pll}}\sin\left(\varphi_{i-}+\varphi_{\theta-}\right)\frac{L_m}{L_s}U_s\omega K_{p1}K_{i3}\Big|_{t_0}^{t_0+\frac{2\pi}{\omega}}\\ &+\frac{1}{2}I_{dr0}\left(I_{-}U_{-} - I_{+}U_{+}\right)K_{\mathrm{pll}}\cos\left(\varphi_{i-}+\varphi_{\theta-}\right)\left(\frac{L_m}{L_s}U_s\frac{K_{i3}K_{i1}}{\omega}\right)\Big|_{t_0}^{t_0+\frac{2\pi}{\omega}}\\ &+\frac{1}{2}I_{dr0}\left(I_{-}U_{-} - I_{+}U_{+}\right)K_{\mathrm{pll}}\sin\left(\varphi_{i-}+\varphi_{\theta-}\right)\left(\frac{L_m}{L_s}U_s K_{i1}K_{p3}+K_{i3}-\omega\omega_2 L_r\right)\Big|_{t_0}^{t_0+\frac{2\pi}{\omega}}\\ &+\frac{1}{2}U_{dr0}\left(I_{-}U_{-} - I_{+}U_{+}\right)K_{\mathrm{pll}}\sin\left(\varphi_{i-}+\varphi_{\theta-}\right)\frac{\left(R_r - U_s K_{p1}K_{p3}\right)\omega_1^2 + U_s K_{i1}K_{i3}}{\omega^2 R_r\cos\varphi - \left(\frac{L_m^2-L_rL_s}{L_s}\right)^2\omega^2\left(\omega_s-\omega_r\right)}\Big|_{t_0}^{t_0+\frac{2\pi}{\omega}} \end{aligned} \tag{37}$$

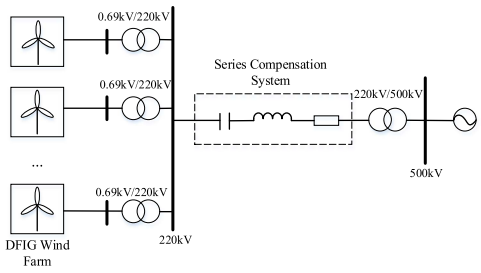

Fig. 5. Diagram of simulation system.

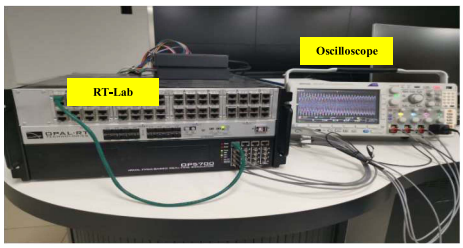

(a)

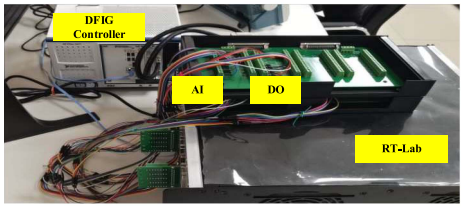

(b)

Fig. 6. Experimental Platform. (a) RT-Lab and oscilloscope. (b) Connection between RT-Lab and DFIG Controller. DFIG controller is an external physical controller that contains control of DFIG rotor-side and grid-side converters and generates converter control signals as input signals to RT-LAB for simulation analysis

In (37) and (39), the items containing PLL parameters (i.e., $K_{\rm pll}$) all appear in the form of product terms in the expressions of $\Delta\eta_{2s1}$ and $\Delta\eta_{2s2}$, thus PLL parameters does not change the sign of dissipation intensity (being positive or negative), but only affect the value of dissipation intensity. Besides, according to (37) and (39), affected by the value of ω and ω_2, when subsynchronous components are dominant, both $\Delta\eta_{2s1}$ and $\Delta\eta_{2s2}$ are below 0. Therefore, decreasing PLL parameters, K_p and $K_{\rm i}$ can lower the negative dissipation effect of stator and excitation channel energy and increase system dissipation intensity, which will weaken system subsynchronous oscillation.

IV. Simulation Verification

To verify the feasibility of the proposed method in a real system, a simulation model is built in RT-LAB, as shown in Fig. 5, and the experimental platform is shown in Fig. 6. In this region, an equivalent wind turbine is integrated to a 220-kV substation, and then is transmitted via two 500-kV series compensation circuits (double-circuit on the same tower). The total capacity of wind power is 3426 MW. DFIG controller is used to regulate the parameters of the large-capacity equivalent wind turbine. Detailed settings of DFIG parameters are shown in Table I.

Three oscillating conditions are set in this article, i.e., diverging oscillation, constant-amplitude oscillation, and converging

TABLE I
DFIG System Parameters

Parameter	Symbol	Value	Parameter	Symbol	Value
Rated power	P_m	3426MW	Rotor resistance	R_r	0.05631pu
Rated frequency	f	50Hz	Stator leakage inductance	Ls	0.1pu
Stator rated voltage	U_s	0.69kV	Rotor leakage inductance	L_r	0.03129pu
Stator resistance	R_s	0pu	Mutual inductance	L_m	0.13129pu
PLL integral parameter	$K_{i\theta}$	38.2pu	GSC inner loop integral parameter	K_{ig3}	10.38pu
PLL proportional parameter	$K_{p\theta}$	0.67pu	GSC inner loop proportional parameter	K_{pg3}	0.98pu
RSC inner loop integral parameter	K_{i3}	4pu	RSC active power outer loop integral parameter	K_{i1}	16pu
RSC inner loop proportional parameter	K_{p3}	0.6pu	RSC active power outer loop integral parameter	K_{p1}	2.2pu

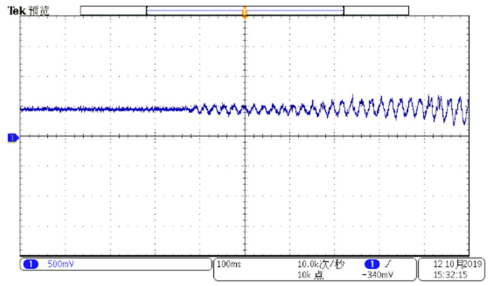

Fig. 7. Active power at the terminal of wind farm in the case of diverging oscillation.

oscillation. According to the measured values of system oscillation components at the terminal of the wind farm, the correctness of dynamic energy function and the feasibility of the proposed stability assessment method are verified. On this basis, combining time-domain simulation, the effect of system parameters on subsynchronous oscillation is assessed comparatively.

A. Model Verification and Stability Assessment

1) Diverging Oscillation: When $t = 2$ s, add a series compensation circuit with 30% series compensation degree to the DFIG-integrated system so that subsynchronous oscillation occurs in the system with the diverging trend. Time-domain curve of active power at the terminal of wind farm is shown in Fig. 7.

Measure the variation of voltage, current, and power at the terminal of wind farm and apply the measured values to (6) so that the measured value of dynamic energy at the terminal of wind farm can be obtained, as shown in blue circles in Fig. 8(a). It can be seen that the calculated value and measured value both exhibit a rising trend and basically coincide with each other. Consider that the measured value contains components of frequencies other than ω, thus it oscillates slightly, but the fluctuation error is within 1.3%.

The variation curves of wind farm terminal dynamic energy, PLL dynamic energy, and transmission line dynamic energy are shown in Fig. 8(b). It can be seen that the dynamic energy of PLL is positive, i.e., PLL generates dynamic energy; the dynamic

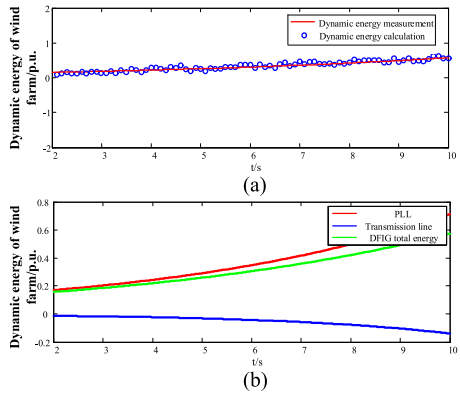

Fig. 8. Dynamic energy of wind farm in the case of diverging oscillation.

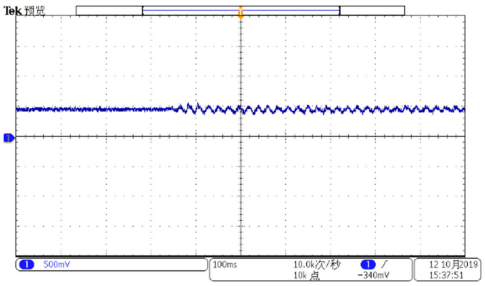

Fig. 9. Active power at the terminal of wind farm in the case of constant-amplitude oscillation.

energy of the transmission line is constantly negative, i.e., the transmission line continuously absorbs dynamic energy. The dynamic energy at the terminal of the wind farm is constantly positive and keeps increasing. According to the stability criteria of dissipation intensity, the value of $\Delta\dot{W}_{\mathrm{DFIG}}(t)$ is constantly positive, thus the system is unstable and system oscillation will diverge, which is consistent with the time-domain simulation result shown in Fig. 7.

2) Constant-Amplitude Oscillation: When $t = 2$s, add a series compensation circuit with 20% series compensation degree to the power grid, so that subsynchronous oscillation with constant amplitude occurs in the system. Time-domain curve of active power at the terminal of wind farm is shown in Fig. 9.

The measured value and calculated value of wind farm dynamic energy are shown in Fig. 10(a). It can be seen that during oscillation the dynamic energy that wind farm generates remains basically unchanged, and the measured value and calculated value of terminal dynamic energy are approximately the same, the maximum error being within 2.1%. The variation curves of wind farm terminal dynamic energy, PLL dynamic energy, and transmission line dynamic energy are shown in Fig. 10(b). It can be seen that, since the variation of voltage and current components in one oscillation period are constant, wind farm dynamic energy and its components are all constant. The energy at the terminal of wind farm is constantly positive, $\Delta\dot{W}_{\mathrm{DFIG}}(t)$ is constantly zero, and the system is in a critical stable state.

3) Converging Oscillation: When $t = 2$s, add a series compensation circuit with 10% series compensation degree to the power grid so that subsynchronous oscillation occurs in the

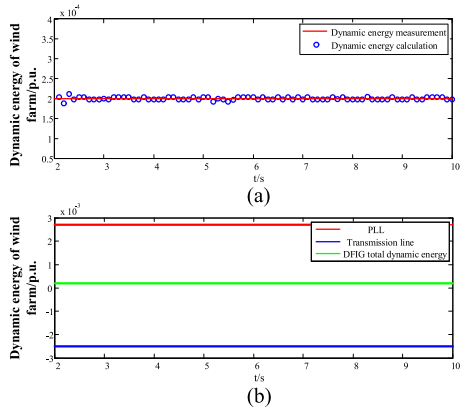

Fig. 10. Dynamic energy of wind farm in the case of constant-amplitude oscillation.

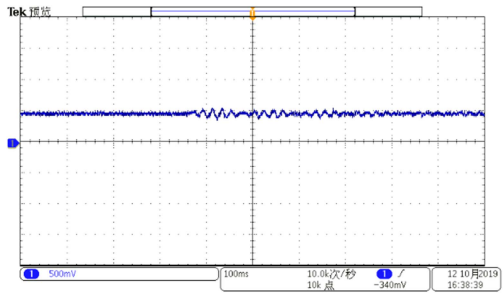

Fig. 11. Active power at the terminal of wind farm in the case of converging oscillation.

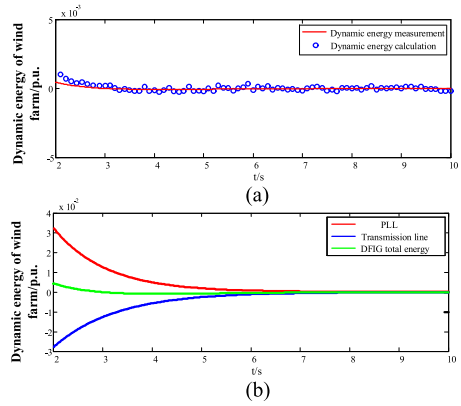

Fig. 12. Dynamic energy of wind farm in the case of converging oscillation.

system which then gradually converges to a stable state. Time-domain curve of active power at the terminal of wind farm is shown in Fig. 11.

In this case, the calculated value and measured value of wind farm dynamic energy are shown in Fig. 12(a). It can be seen that wind farm dynamic energy and its components all exhibit a descending trend. As the oscillation converges, the dynamic energy gradually decreases, and when the system reaches a stable state, the dynamic energy is next to zero. Besides, the measured value and calculated value remain consistent, the error being within 2.0%.

TABLE II
SIMULATION DATA OF WIND FARM DISSIPATION INTENSITY IN FIGS. 7, 9, AND 11

Case	Calculated value	Measured value	Error
Diverging oscillation	-1.45	-1.455	3.4%
Constant-amplitude oscillation	0	$7.76*10^{-5}$	-
Converging oscillation	0.8	0.82	2.4%

The variation trends of wind farm dynamic energy and its components are shown in Fig. 12(b). In this case, the absolute values of the dynamic energy that PLL generates and the dynamic energy that transmission line absorbs both exhibit gradually descending trend. It means the dynamic energy that wind farm generates gradually decreases, $\Delta \dot{W}_{\mathrm{DFIG}}(t)$ is constantly negative, and the system is stable.

4) Quantitative Analysis of Stability Level of Wind Farm Dynamic Energy: Concerning the above three operating conditions, two different methods are utilized to assess the stability level of DFIG-integrated system, i.e., by calculating the gradient of dynamic energy to obtain the dissipation intensity and by using the measured values to fit the dissipation intensity online. The results are shown in Table II.

It can be seen that the maximum error between the measured value and calculated value is only 3.4%. Besides, in the first case, the dissipation intensity of wind farm is negative, i.e., the wind farm continuously injects dynamic energy to the grid, with the value of dynamic energy gradually increasing, thus the system is unstable and oscillates to divergence. In the second case, the dissipation intensity of the system is next to zero, i.e., the wind farm continuously injects constant dynamic energy to the grid, thus the system is critical stable. In the third case, the dissipation intensity is positive, thus the dynamic energy that wind farm generates gradually decreases, and the system gradually inclines to be stable.

B. Stability Assessment With Different System Parameters

On the basis of theoretical analysis, through time-domain simulation verification, stability assessment with different system parameters is further explored.

1) Series Compensation Degree of Transmission Line: According to the analysis in Section IV, series compensation degree and line resistance mainly affect the dissipation intensity of the transmission line, thus affecting the overall stability level of the DFIG-integrated power system. Apply different values of system control parameters and operation parameters to the model of dissipation intensity, i.e., the series compensation degree increasing from 10% to 90% and line resistance increasing from 0.031 to 0.279 p.u. The effects of different values of series compensation degree and line resistance on the dissipation intensity are shown in Fig. 13. It can be seen that as the series compensation degree increases, system dissipation intensity gradually decreases; while as line resistance increases, system dissipation intensity gradually increases.

To verify the accuracy of the above evaluation results, time-domain simulation tests are conducted concerning two points

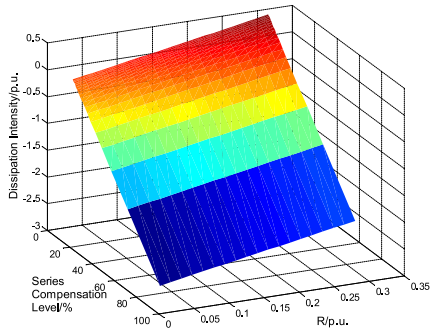

Fig. 13. Effects of line resistance and series compensation degree on DFIG dissipation intensity.

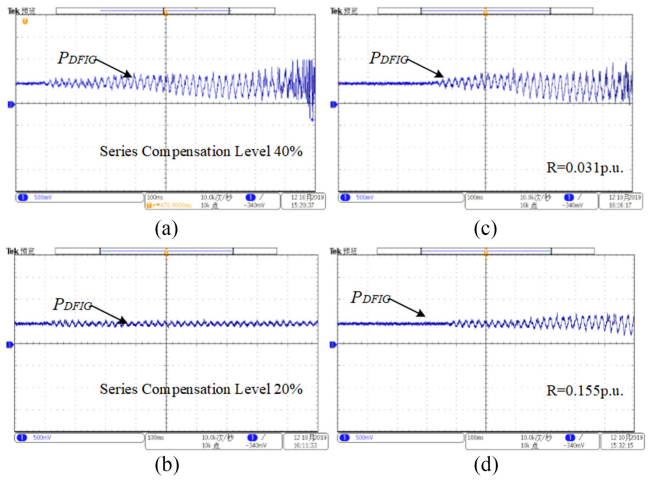

Fig. 14. Experimental results corresponding to different values of line resistance and series compensation degree. (a) Series compensation degree being 20%. (b) Series compensation degree being 40%. (c) Line resistance being 0.031 p.u. (d) Line resistance being 0.155 p.u.

in Fig. 14, i.e., line resistance being 0.279 p.u. and the series compensation degree being 20% and 40%, respectively. The active power of wind farm P_{DFIG} is measured, as shown in Fig. 14(a) and (b). When the series compensation is 20%, it can be seen from Fig. 13 that the dissipation intensity of DFIG is positive and the stability level of the system is positive. In this case, the oscillation of P_{DFIG} gradually converges. When the series compensation degree is 40%, according to the result of stability evaluation, the stability level of the system is negative at this time, and the oscillation of P_{DFIG} diverges acutely and the system goes unstable. Such simulation results are consistent with the stability evaluation results.

Fig. 14(c) and (d) are the time-domain simulation results when the series compensation degree is 40% and line resistance is 0.155 and 0.031 p.u., respectively. When $R = 0.155$ p.u., system oscillation diverges slowly. When line resistance decreases to 0.031 p.u., system oscillation exhibits obvious diverging trend and finally goes unstable. According to the stability evaluation results of dissipative strength in Fig. 13, the stability level at $R = 0.155$ p.u. is greater than that at $R = 0.031$ p.u., while the stability level of the two is still negative. The evaluation results are consistent with the stability evaluation results.

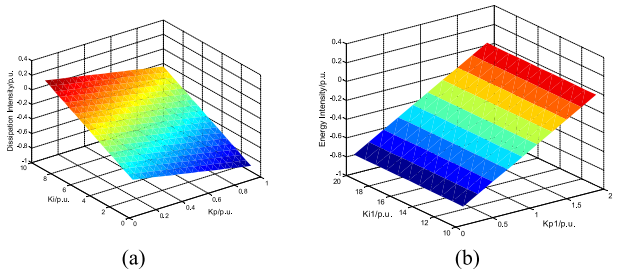

Fig. 15. Effects of inner-loop and outer-loop control parameters of rotor-side converters on the dissipation intensity. (a) Effect of inner-loop control parameters. (b) Effect of outer-loop control parameters.

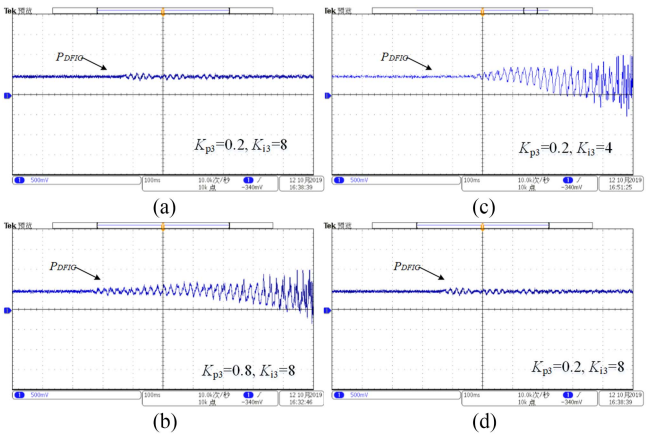

Fig. 16. Experimental results corresponding to different values of current inner-loop control parameters. (a) $K_{p3} = 0.2$ and $K_{i3} = 8$. (b) $K_{p3} = 0.8$ and $K_{i3} = 8$. (c) $K_{p3} = 0.2$ and $K_{i3} = 4$. (d) $K_{p3} = 0.2$ and $K_{i3} = 8$.

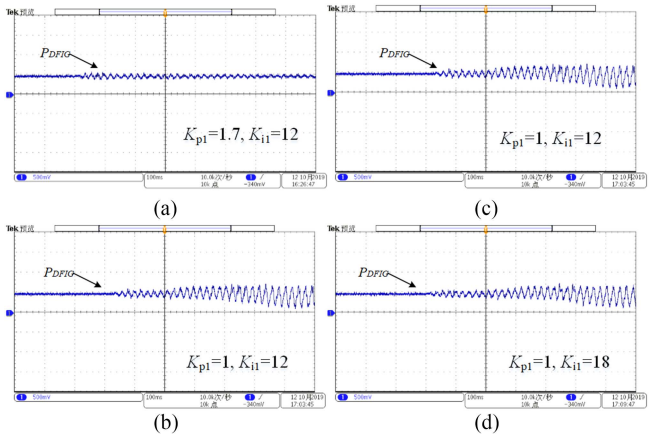

Fig. 17. Experimental result curves corresponding to different values of outer-loop control parameters. (a) $K_{p1} = 1.7$ and $K_{i1} = 12$. (b) $K_{p1} = 1$ and $K_{i1} = 12$. (c) $K_{p1} = 1$ and $K_{i1} = 12$. (d) $K_{p1} = 1$ and $K_{i1} = 18$.

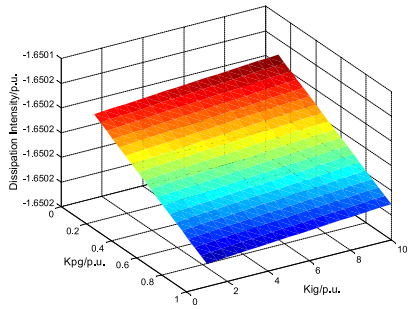

Fig. 18. Effects of inner-loop control parameters of grid-side converters on the dissipation intensity.

2) Converter Control Parameters: The effects of current inner-loop and outer-loop control parameters of the rotor-side converter on the dissipation intensity are shown in Fig. 15, where Fig. 15(a) depicts the pattern in which rotor-side converter inner-loop control affects the dissipation intensity of the DFIG-integrated system. It can be seen that increasing K_{i3} or decreasing K_{p3} can increase system dissipation intensity and improve the stability margin. Fig. 15(b) depicts the effects of rotor-side converter outer-loop control parameters on system dissipation intensity. It can be seen that the dissipation intensity is scarcely affected by the outer-loop integration gain, but only increases as proportion gain K_{p1} increases.

Based on the above dissipation intensity analysis, different values of rotor-side converter inner-loop parameters are selected for experimental tests. The oscillation curves of DFIG active power corresponding to different parameters are shown in Fig. 15. When inner-loop proportion parameter K_p increases from 0.2 to 0.8, the oscillation curves are shown in Fig. 16(a) and (b). It can be seen that as K_p increases, system oscillation turns from converging to diverging, which corresponds to the value of dissipation intensity turning from positive to negative in Fig. 15, i.e., system stability level is lowered. When inner-loop integration parameter K_i increases from 4 to 8, the oscillation curves are shown in Fig. 16(c) and (d). It can be seen that as K_i increases, system oscillation gradually converges, i.e., system stability level is improved. This is consistent with the above stability assessment result.

Furthermore, the effectiveness of stability assessment corresponding to different values of rotor-side converter outer-loop control parameters is verified, and the experimental results are shown in Fig. 17. When the value of outer-loop proportion parameter K_{p1} is, respectively, 1.7 and 1, the oscillation curves are shown in Fig. 17(a) and (b). It can be seen that when $K_{p1} = 1$, system oscillation diverges, which corresponds to the value of dissipation intensity being negative in Fig. 15. When K_{p1} increases to 1.7, system oscillation converges, which corresponds to the dissipation intensity turning positive, i.e., system stability level is improved. When the value of outer-loop integration parameter K_{i1} is, respectively, 12 and 18, the oscillation curves are shown in Fig. 17(c) and (d). It can be seen that when the value of K_{i1} varies, the system oscillation trend does not exhibit any obvious change, which corresponds to the value of dissipation intensity remaining negative in Fig. 15. Such simulation result is consistent with the above stability assessment result.

The effects of current control parameters of the grid-side converter on the dissipation intensity are shown in Fig. 18. Grid-side inner converter control parameters have the same effect on the dissipation intensity as rotor-side converter control parameters. However, when grid-side converter control parameters vary, the variation amplitude of dissipation intensity is much smaller

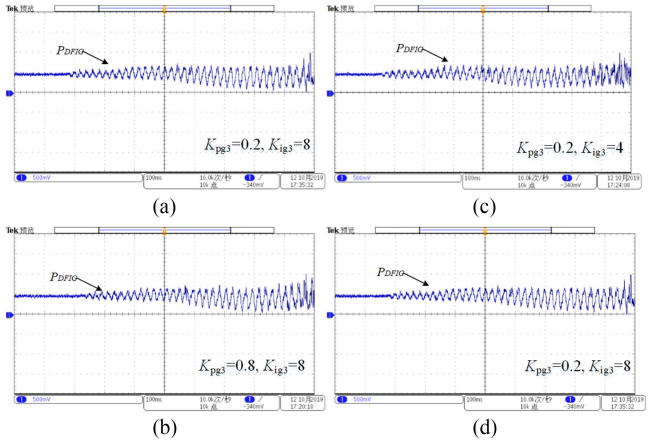

Fig. 19 Experimental results corresponding to different values of grid-side converter control parameters. (a) $K_{pg3} = 0.2$ and $K_{ig3} = 8$. (b) $K_{pg3} = 0.8$ and $K_{ig3} = 8$. (c) $K_{pg3} = 0.2$ and $K_{ig3} = 4$. (d) $K_{pg3} = 0.2$ and $K_{ig3} = 8$.

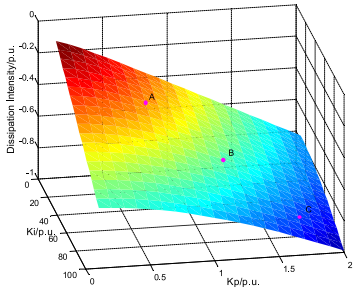

Fig. 20. Effect of PLL parameters on DFIG dissipation intensity.

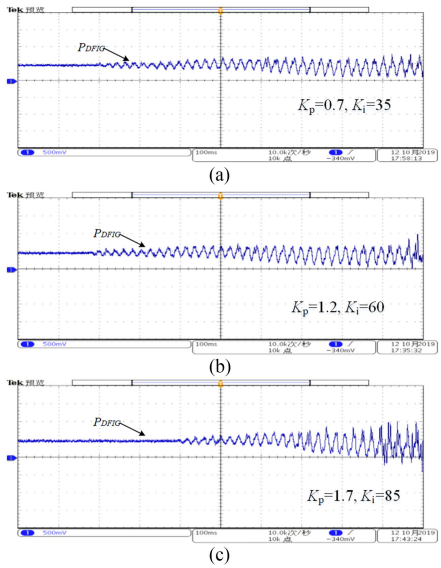

Fig. 21. Experimental results corresponding to PLL parameters of point A, B, and C.

than when rotor-side converter control parameters vary, i.e., the stability level of DFIG subsynchronous oscillation is mainly affected by rotor-side converter control parameters.

The experimental results corresponding to different values of grid-side converter inner-loop control parameters are shown in Fig. 19. It can be seen that changing grid-side converter inner-loop control parameters has no obvious effect on system oscillation, which corresponds to the value of dissipation intensity remaining almost the same in Fig. 18.

3) PLL Control Parameters: PLL control parameters can affect the dissipation intensity generated by PLL, thus affecting system stability. Corresponding to different values of control parameters, the variation trend of wind farm dissipation intensity is depicted, as shown in Fig. 20, where parameter K_p increases from 0.1 to 2 and parameter K_i increases from 10 to 100. It can be seen that, as K_p and K_i increase, system dissipation intensity gradually drops.

Concerning the effect of different PLL control parameters on wind farm dissipation intensity, time-domain simulation tests are conducted concerning three groups of control parameters in Fig. 21, i.e., *A* ($K_p = 0.7$, $K_i = 35$), *B* ($K_p = 1.2$, $K_i = 60$), and *C* ($K_p = 1.7$, $K_i = 85$). According to Fig. 20, the relationship between the stability levels of three groups of control parameters is as follows: A $>$ B $>$ C. However, due to the negative stability levels of the three groups, only the divergence velocity and the oscillation amplitude are different. It can be seen that when K_p and K_i are relatively big, system oscillation diverges and goes unstable, as shown in the blue line. When K_p and K_i drop, the oscillation amplitude of phase-locked angle also gradually drops, and system oscillation slightly converges. When $K_p = 0.7$ and $K_i = 35$, system oscillation has smaller amplitude than in the former two cases. Therefore, by decreasing PLL control parameters, system stability level can be improved. Such simulation results are consistent with the stability assessment results.

V. Conclusion

In this article, the model of DFIG dynamic energy that reflects the characteristic of subsynchronous oscillation is constructed, system dissipation intensity is defined according to Lyapunov stability criteria, and the stability level of system subsynchronous oscillation is quantified. On this basis, the detailed expression of DFIG dissipation intensity is analyzed, thus the pattern in which the series compensation degree and PLL parameters affect system subsynchronous oscillation is explored. The following conclusions can be reached.

1) DFIG terminal dynamic energy contains two components, one of which is determined by the external network and the other one is determined by internal control links. The dynamic energy component determined by the external network is mainly affected by the grid-side series compensation system and line parameters. The dynamic energy component determined by internal control links is mainly affected by parameters of PLL, rotor-side converter, and grid-side converter.
2) The negative gradient of DFIG dynamic energy is defined as the dissipation intensity. According to the Lyapunov stability theory, the quantified stability criteria of DFIG subsynchronous oscillation are constructed. When the dissipation intensity is positive, system oscillation converges, and the bigger the dissipation intensity is, the higher the system stability level is. When the dissipation intensity is

zero, constant-amplitude oscillation occurs in the system, and the system is critical stable. When the dissipation intensity is negative, system oscillation diverges, and the smaller the dissipation intensity is, the lower the system stability level is.

3) The proposed online stability assessment scheme can assess the degree in which different system parameters affect the stability of subsynchronous oscillation. The proportion and integration control parameters of the DFIG rotor inner loop, the proportion parameter of the DFIG rotor outer loop, PLL parameters, line resistance, and series compensation degree are key factors that affect the system stability level. By reducing rotor-side converter inner-loop proportion gain and PLL parameters or increasing inner-loop integration gain and outer-loop proportion gain, system dissipation intensity can be increased, thus system stability level can be improved. Increasing line resistance or decreasing the series compensation degree can also improve the stability level of system.

REFERENCES

[1] W. Du, Q. Fu, H. Wang, and Y. Wang, "Concept of modal repulsion for examining the subsynchronous oscillations caused by wind farms in power systems," *IEEE Trans. Power Syst.*, vol. 34, no. 1, pp. 518–526, Jan. 2019.

[2] K. Gu, F. Wu, and X. Zhang, "Sub-synchronous interactions in power systems with wind turbines: A review," *IET Renewable Power Gener.*, vol. 13, no. 1, pp. 4–15, 2019.

[3] Y. Cheng, M. Sahni, D. Muthumuni, and B. Badrzadeh, "Reactance scan crossover-based approach for investigating SSCI concerns for DFIG-based wind turbines," *IEEE Trans. Power Del.*, vol. 28, no. 2, pp. 742–751, Apr. 2013.

[4] M. S. Annakkage, C. Karawita, and U. D. Annakkage, "Frequency scan-based screening method for device dependent sub-synchronous oscillations," *IEEE Trans. Power Syst.*, vol. 31, no. 3, pp. 1872–1878, May 2016.

[5] S. Wang and Z. Xu, "Increasing the SSO damping effectiveness of IMDU by raising its operating frequency and optimizing its parameters," *IEEE Trans. Power Syst.*, vol. 28, no. 3, pp. 3134–3144, Aug. 2013.

[6] J. Sun, "Impedance-based stability criterion for grid-connected inverters," *IEEE Trans. Power Electron.*, vol. 26, no. 11, pp. 3075–3078, Nov. 2011.

[7] H. Liu, X. Xie, C. Zhang, Y. Li, H. Liu, and Y. Hu, "Quantitative SSR analysis of series-compensated DFIG-based wind farms using aggregated RLC circuit model," *IEEE Trans. Power Syst.*, vol. 32, no. 1, pp. 474–483, Jan. 2017.

[8] M. Wu, L. Xie, L. Cheng, and R. Sun, "A study on the impact of wind farm spatial distribution on power system sub-synchronous oscillations," *IEEE Trans. Power Syst.*, vol. 31, no. 3, pp. 2154–2162, May 2016.

[9] W. Chen, D. Wang, X. Xie, J. Ma, and T. Bi, "Identification of modeling boundaries for SSR studies in series compensated power networks," *IEEE Trans. Power Syst.*, vol. 32, no. 6, pp. 4851–4860, Nov. 2017.

[10] X. Zhu, H. Sun, J. Wen, and S. Cheng, "Improved complex torque coefficient method using CPCM for multi-machine system SSR analysis," *IEEE Trans. Power Syst.*, vol. 29, no. 5, pp. 2060–2068, Sep. 2014.

[11] A. Tabesh and R. Iravani, "On the application of the complex torque coefficients method to the analysis of torsional dynamic," *IEEE Trans. Energy Convers.*, vol. 20, no. 2, pp. 268–275, Jun. 2005.

[12] L. Shi and G. Xu, "Sub-synchronous resonance analysis and simulation on wind farm," in *Proc. 2nd Int. Conf. Power Renewable Energy* , 2017, pp. 412–416.

[13] M. Zhang *et al.*, "Discussion on on-line identification and warning of subsynchronous oscillation for phasor measuring unit," *Autom. Elect. Power Syst.*, vol. 40, no. 16, pp. 143–152, 2016.

[14] Z. Yan *et al.*, "An overall theoretical description of frequency slice wavelet transform," *Mech. Syst. Signal Process.*, vol. 24, no. 2, pp. 491–507, 2010.

[15] Y.-H. Moon, B.-H. Cho, Y.-H. Lee, and H.-S. Hong, "Energy conservation law and its application for the direct energy method of power system stability," in *Proc. IEEE Power Eng. Soc. Winter Meet.*, 1999, vol. 1, pp. 695–700.

[16] I. Vieto and J. Sun, "Small-signal impedance modelling of type-III wind turbine," in *Proc. IEEE Power Energy Soc. Gen. Meet. IEEE*, 2015, pp. 1–5.

[17] R. Fang, W. Chen1, X. Zhang, and D. Xu, "Improved virtual inductance based control strategy of DFIG under weak grid condition," in *Proc. Int. Power Electron. Conf.*, 2018, pp. 4213–4219.

[18] L. Wang, X. Xie, Q. Jiang, H. Liu, Y. Li, and H. Liu, "Investigation of SSR in practical DFIG-Based wind farms connected to a series-compensated power system," *IEEE Trans. Power Syst.*, vol. 30, no. 5, pp. 2772–2779, Sep. 2015.

[19] W. Ning, X. Wu, Y. J. Guan, and F. Chen, "Method to suppress sub-synchronous oscillation of DFIG-based wind farms based on virtual impedance," *J. Eng.*, vol. 2017, no. 13, pp. 2173–2177, 2017.

Jing Ma (Senior Member, IEEE) received the B.S. and Ph.D. degree from North China Electric Power University, Beijing, China, in 2003 and 2008, respectively.

He has been a Visiting Research Scholar with the Bradley Department of Electrical and Computer Engineering, Virginia Polytechnic Institute and State University from 2008 to 2009. He is currently a Professor with the School of Electrical and Electronic Engineering, North China Electric Power University, China. His major research interests include power system stability and control.

Yaqi Shen (Member, IEEE) was born in Jiangsu Province, China. She is currently working toward the Ph.D. degree with the School of Electrical and Electronic Engineering, North China Electric Power University, Beijing, China.

Her research interests mainly include power system stability analysis and control.